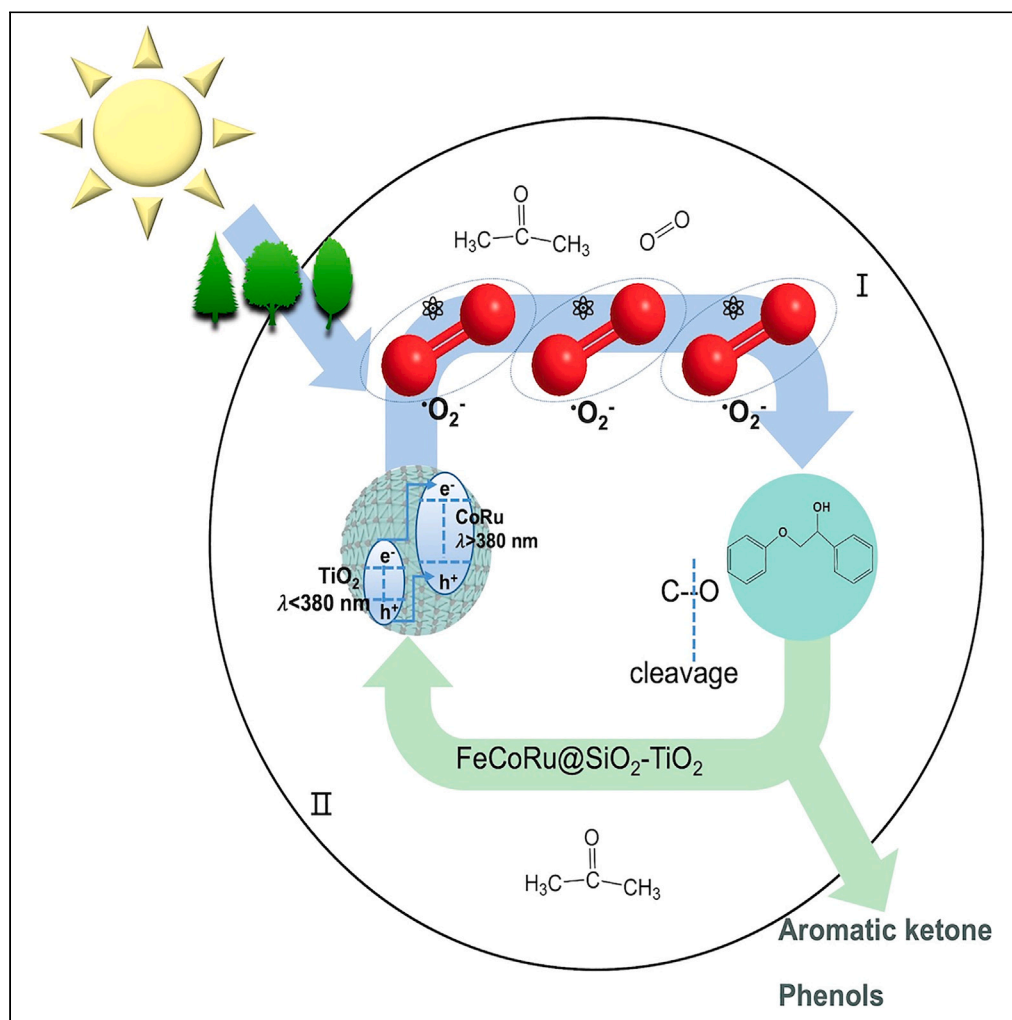**Article**

Multisite photocatalytic depolymerization of lignin model compound utilizing full-spectrum light over magnetic microspheres

Chengcheng Suo,
Wei Li, Sha Luo,
Chunhui Ma,
Shouxin Liu

mchmchmchmchmch@163.com
(C.M.)
liushouxin@126.com (S.L.)

Highlights

High lignin
depolymerization
efficiency by a magnetic
microsphere multisite
photocatalyst

O_2^- is the key to break the
β-O-4 bond in lignin model
compound

Exploring the mechanism
of the lignin
depolymerization on the
full-spectrum light

Article

Multisite photocatalytic depolymerization of lignin model compound utilizing full-spectrum light over magnetic microspheres

Chengcheng Suo,[1] Wei Li,[1] Sha Luo,[1] Chunhui Ma,[1,2,*] and Shouxin Liu[1,*]

SUMMARY

Photocatalytic depolymerization is a high value-added approach for utilization of lignin. In this study, magnetic microspheres of FeCoRu@SiO$_2$–TiO$_2$ were synthesized by a co-precipitation method. Doping with CoO$_x$ and RuO$_x$ was used to improve the response to visible light, and doping with TiO$_2$ was used to improve the response to ultraviolet light (λ < 380 nm). The lignin model compound depolymerization rate was >90%. The electron paramagnetic resonance results showed that the reaction occurred in two steps (aerobic phase and oxygen-free phase). Most of the O$_2^-$ was produced in the first step by cleavage of C-O bonds. The second step was inhibited in an oxygen-free atmosphere. This research provides a valid method for enhancing the photocatalytic properties using full-spectrum light and exploring the lignin photocatalytic depolymerization mechanism. Further research is required to develop the catalyst properties and performance to produce radicals.

INTRODUCTION

Depolymerization of lignin to produce value-added[1] chemicals provides a pathway to realize a green chemical economy.[2] Because it is an abundant and sustainable resource, lignin has been investigated extensively.[3,4] Currently, pyrolytic,[5] biocatalytic,[6] photocatalytic,[7] and electroncatalytic[8] methods are used for lignin depolymerization.[9] Taking a long-time view, the utilization of lignin has a large potential.[10] Recently, a lot of research has done a lot of works in using new solution (such as deep eutectic solvent, DES),[11] new materials, etc. Besides, photocatalytic depolymerization of lignin is a green and economic method.[12,13] Photocatalytic processes are usually accompanied by electron transfer and formation of holes.[14] Recently, Li et al. developed a strategy for controlled engineering of Cu$_2$O to selectively extract holes and map charge transfer processes at the single-particle level.[15] They verified that electron transfer occurred to the atom surface. Unique reactive species and photogenerated reactive species can attack target chemical bonds under mild conditions.[16] Photogenerated radicals can photocatalytically activate C-O/C-C bonds.[17,18]

Metal oxides (Bi, Ce, Co, Ru, Cu, and Ti)[19–22] have been widely applied in photocatalysis. To achieve this, polymers have been modified with magnetic nanoparticles or doped with single metal atoms. However, the response of single metal atoms to full-spectrum light is limited and there have been few reports of co-doped magnetic catalysts. Recently, Gao et al.[23] reported a Ru-doped amorphous-silica and demonstrated a synergistic interaction between acidic components and the metal. This catalyst could convert lignin-derived monophenols to cyclohexane with high efficiency and yields. Zhang et al.[24] reported a CuO/BiVO$_4$ catalyst that could selectively cleave C$_\alpha$–C$_\beta$ bonds. With the photocatalyst, lignin β-O-4 linkages were broken to form aromatic compounds with a yield of 86.5%. Luo et al.[25] reported a dual light wavelength switching strategy to selectively attack β-O-4 bonds using TiO$_2$ and Pd/ZnInS$_4$, which produced ketones and phenols with a 90% yield. Metal loading experiments and electron paramagnetic resonance (EPR) spectroscopy have been used to elucidate that Ti^{3+} is formed *in situ* and is involved in electron transfer for photocatalytic hydrogenolysis of β-O-4 ketones. β-O-4 bonds are the most common linkages in lignin. Therefore, photocatalytic selective cleavage of β-O-4 bonds is the main step for depolymerization of lignin. Recovery and recycling of catalysts are important, and a catalyst needs to be developed that is easy to recycle and has high selectivity for β-O-4 bonds.

For recovery of the catalyst, magnetic separation is a viable method.[26] Incorporation of Fe$_3$O$_4$ nanoparticles into a catalyst can make it magnetic. However, oxidation of Fe$_3$O$_4$ can occur under irradiation and cause photocorrosion of the catalyst and reduce the transformation efficiency.[12] A core-shell structure of a compound such as SiO$_2$ around Fe$_3$O$_4$ could protect the Fe$_3$O$_4$ from oxidation.

EPR can be used to identify free radicals involved in biomass photocatalytic depolymerization.[27] To date, various compounds (e.g., 5,5-dimethyl-1-pyrroline N-oxide [DMPO], 2,2,6,6-Tetramethylpiperidinooxy [TEMPO], and 5-(Diethoxyphosphoryl)-5-methyl-1-pyrroline N-oxide [DEPMPO]) have been used for spin trapping.[28] DMPO has been the most widely used because it produces stable nitrone and ·O$_2^-$ radical spin adducts.[29] Benzyl radicals, superoxide radicals, hydroxyl radicals, hydroperoxide radicals, and sulfate radicals have been detected

[1]Key Laboratory of Bio-based Material Science and Technology (Ministry of Education), College of Material Science and Engineering, Northeast Forestry University, Harbin 150040, China
[2]Lead contact
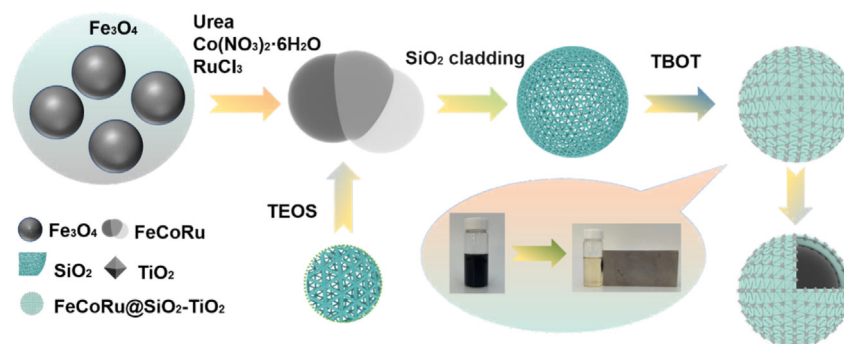*Correspondence: mchmchmchmch@163.com (C.M.), liushouxin@126.com (S.L.)

Figure 1. Synthesis of the FeCoRu@SiO$_2$–TiO$_2$ catalyst.

by EPR to characterize radical degradation of lignin. Zhang et al.[30] reported a method for photocatalytic degradation of lignin to aromatic chemicals using an adjacent functional group modification strategy or modification and radical intermediate mechanism for lignin linkage cleavage.

In the present research, we synthesized a series of catalysts containing magnetic nanoparticles. Scanning transmission electron microscopy (SEM), transmission electron microscopy (TEM), and Fourier transform infrared (FTIR) spectroscopy were used to evaluate the shape of the nanoparticles and determine whether a thin layer of SiO$_2$ was successfully coated on the surface. Powder X-ray diffraction (XRD) was used to determine whether the core of the catalyst was Fe$_3$O$_4$. X-ray photoelectron spectroscopy (XPS) was used to study the oxidation states of the elements and evaluate production of ·O$_2^-$. Additionally, EPR was used to evaluate the photocatalytic activity of FeCoRu@SiO$_2$– TiO$_2$. High-performance liquid chromatography mass spectrometry (HPLC-MS) was used to determine the yields of products formed from FeCoRu@SiO$_2$–TiO$_2$.

RESULTS AND DISCUSSION

Preparation of the catalyst

RuCl$_3$·3H$_2$O and Co (NO$_3$)$_2$·6H$_2$O were deposited on Fe$_3$O$_4$ nanoparticles using a co-precipitation method with urea as a co-precipitant. First, the Fe$_3$O$_4$ (0.01 mol) was mixed with ultrapure water by ultrasonication. Next, RuCl$_3$·3H$_2$O (0.52 g), Co (NO$_3$)$_2$·6H$_2$O (2.91 g), and urea (108.22 g) were mixed with 50.0 mL of ultrapure water under stirring and then mixed with the Fe$_3$O$_4$ solution for 10 h at 25°C and another 10 h at 90°C. The mixture was then left for 18 h. The obtained sample was washed with ultrapure water three times and ethanol three times and then vacuum dried for 24 h at 60°C and labeled as FeCoRu.

The FeCoRu was mixed with 95% ethanol (200 mL) by ultrasonication. Then 15.0 mL of ultrapure water and 30.0 mL of ammonium hydroxide were added with stirring at 25°C. Tetraethyl orthosilicate (TEOS) (10 mL) was added dropwise to the solution over 2 h, and then the mixture was left to react for 5 h. The obtained sample by magnetic separating was washed with ultrapure water three times and ethanol three times and then vacuum dried for 24 h at 60°C and labeled as FeCoRu@SiO$_2$.

The obtained FeCoRu@SiO$_2$ was mixed with 95% ethanol (200 mL) by ultrasonication to prepare solution A. Solution B was prepared by mixing 20.0 mL of ethanol with 8.0 mL of tetrabutyl titanate and 60.0 mL of isopropyl alcohol. Then solution B was added dropwise to solution A over 2 h at 70°C and the mixture was reacted for 10 h. The obtained sample by magnetic separating was washed with ultrapure water three times and ethanol three times and then vacuum dried for 24 h at 60°C. Finally, the resulting solid was calcined in a muffle furnace at 500°C for 2 h in air and labeled as FeCoRu@SiO$_2$–TiO$_2$ (Figure 1).

FeCoBi@SiO$_2$–TiO$_2$, FeCoCe@SiO$_2$–TiO$_2$, and FeCoCu@SiO$_2$–TiO$_2$ were synthesized by the same method but using 0.01 mol of Bi (NO$_3$)$_2$·5H$_2$O, 0.01 mol of Ce (NO$_3$)$_3$·6H$_2$O, and 0.01 mol of Cu (NO$_3$)$_2$·6H$_2$O, respectively, in place of the RuCl$_3$·3H$_2$O.

Characterization of the catalyst

The morphologies of the magnetic nanocomposites were studied using a Leica inverted fluorescence microscope and SEM. The catalysts in the solvents were first observed using the Leica inverted fluorescence microscope, which showed they had excellent dispersibility (Figure S1). The SEM results showed that the particles were uniform in shape and size (Figures 2A–2F). The particle sizes of FS@TiO$_2$–Co and FeCoRu@SiO$_2$– TiO$_2$ were approximately 400 and 800 nm, respectively. The FeCoRu@SiO$_2$–TiO$_2$ particles were more evenly distributed than the FS@TiO$_2$–Co particles (Figure 2D). The SEM images (Figures 2B, 2C, 2E, and 2F) of the nanocomposite showed it was a metal oxide,[31,32] with CoO$_x$ and TiO$_x$ on the surface. Energy dispersive spectroscopy (EDS) was used for elemental analysis of the FeCoRu@SiO$_2$–TiO$_2$ (Figures S2 and S3). The major elements in FS@TiO$_2$–Co were O (48%), Ti (45%), Fe (45%), and Co (4%). The major elements in FeCoCe@SiO$_2$–TiO$_2$ were O (32%), Ti (19%), Ce (18%), Fe (17%), and Co (14%). These results showed that the Co and Ti contents in FeCoCe@SiO$_2$–TiO$_2$ were higher than those in FS@TiO$_2$–Co. The contents of Co and Ti increased with the co-precipitation method (Figures S2 and S3).
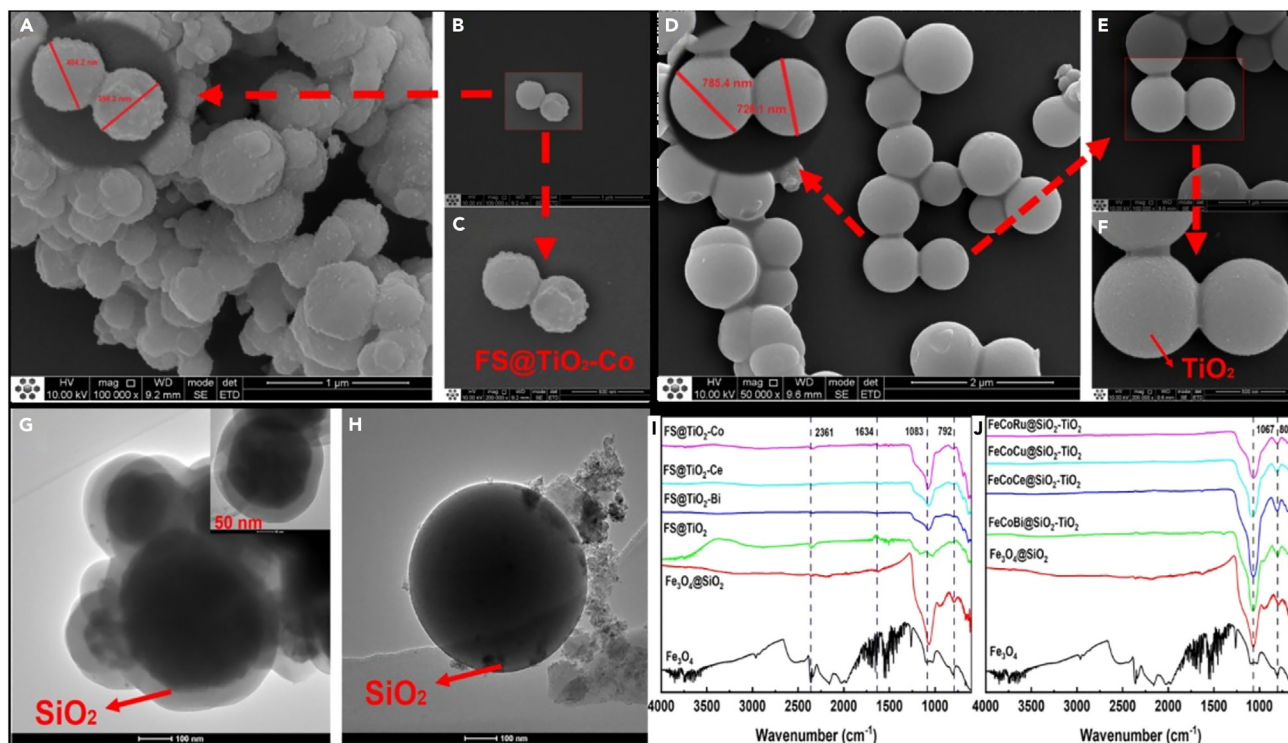
Figure 2. SEM images of Fe$_3$O$_4$@SiO$_2$@TiO$_2$–Co (FS@TiO$_2$–Co) and FeCoRu@SiO$_2$–TiO$_2$

(A–J) The scale bars represent 2 μm (A and D), 1 μm (B and E), and 500 nm (C and F). TEM images of FS@TiO$_2$–Co (G) and FeCoRu@SiO$_2$–TiO$_2$ (H). The scale bars represent 100 nm (A and B). FT-IR spectra of FS, FS@TiO$_2$, FS@TiO$_2$–Bi, FS@TiO$_2$–Ce, and Fs@TiO$_2$–Co prepared by the sol-gel method (I) and the co-precipitation method (J).

The TEM results (Figures 2G and 2H) for FS@TiO$_2$–Co and the FeCoRu@SiO$_2$–TiO$_2$ showed that SiO$_2$ was successfully coated on the FeCoRu and Fe$_3$O$_4$ nanoparticles. Two different regions with distinct electron densities were observed (Figures 2G and 2H), which confirmed that a core-shell structure was formed successfully.[33]

The FTIR spectra (Figure 2I) confirmed that TiO$_2$ and other metal oxides formed on the surface. After vacuum drying, the obtained samples had many OH groups on the SiO$_2$. After calcination, the peak for OH at approximately 3422 cm^{-1} disappeared. Peaks related to the Si-O-Si bond in SiO$_2$ were located at approximately 1067 and 1083 cm^{-1} (Figures 2I and 2J), which indicated that a SiO$_2$ layer was created on FeCoX (where X is Bi, Ce, Cu, or Ru) and Fe$_3$O$_4$. The peaks at 792, 800, and 400–800 cm^{-1} (Figure 2I) were related to the Ti-O bond and showed that some of the Si-O-Si bonds were replaced with Ti-O bonds.[34,35]

Most aqueous solutions of metal salts have a pH of <7; for example, the pH of an aqueous RuCl$_3$ solution is pH < 1. The Fe$_3$O$_4$ could react with these solutions. In our results, the XRD patterns of the catalysts showed diffraction peaks at approximately 2θ of 10°–80°, which were consistent with the standard for Fe$_3$O$_4$ (PDF#75–0449). For Fe$_3$O$_4$, the XRD pattern showed typical peaks for Fe$_3$O$_4$ phases at 2θ of 30.1°, 35.5°, 43.5°, 53.4°, 57.0°, and 62.6°,[36] corresponding to the 220, 311, 400, 422, 511, and 411 lattice planes, respectively. These results confirmed that the Fe$_3$O$_4$ phases were retained (Figures 3A–3C). No changes were detected in the phase composition after addition of other metals, which could be highly dispersed in the Fe$_3$O$_4$ microspheres.[37]

Surface metal states and metal oxygen species

XPS was used to determine the oxidation states of the metal catalysts. Our XRD results proved that the complete lattice of Fe$_3$O$_4$ was retained. The survey XPS spectrum of FeCoRu@SiO$_2$–TiO$_2$ is shown in Figure 3. The Co 2p peak was split into four peaks at 779.1, 783.9, 794.9, and 800.9 eV (Figure 3F). The peaks at 783.9 and 800.9 eV corresponded to Co 2p$_{3/2}$ and Co 2p$_{1/2}$, respectively, which are characteristic of the Co^{2+} valence state in FeCoRu@SiO$_2$–TiO$_2$.[38–40] The peaks at 779.1 and 794.9 eV were for Co^{3+}, which was produced by surface oxidation. Peaks for Ru 3 d in FeCoRu@SiO$_2$–TiO$_2$ appeared at 285.0 eV (Ru 3d$_{3/2}$) and 280.8 eV (Ru 3d$_{5/2}$).[41–43] The Ru 3d$_{3/2}$ peak overlapped with the C 1s peak at 284.8 eV. The peaks at approximately 280.8 eV (Figure 3E) showed that RuO$_x$ species were present. The observed RuO$_x$ species are presumably produced on the surface of FeCoRu@SiO$_2$–TiO$_2$ by oxidation of Ru^0 or Ru^{3+} species when the catalyst is calcined in air.[44] Doped Ti is more likely to be located at the surface or near the surface of Si-O and will form octahedral TiO$_2$. An increase in oxygen vacancies in FeCoRu@SiO$_2$–TiO$_2$ was confirmed by O 1s XPS (Figure 3D) and EPR. The position of oxygen vacancies is directly related to the crystal form of TiO$_2$, with oxygen vacancies tending to exist in the bulk phase of anatase TiO$_2$ and on the surface layer of rutile TiO$_2$.[45] Surface-layer oxygen
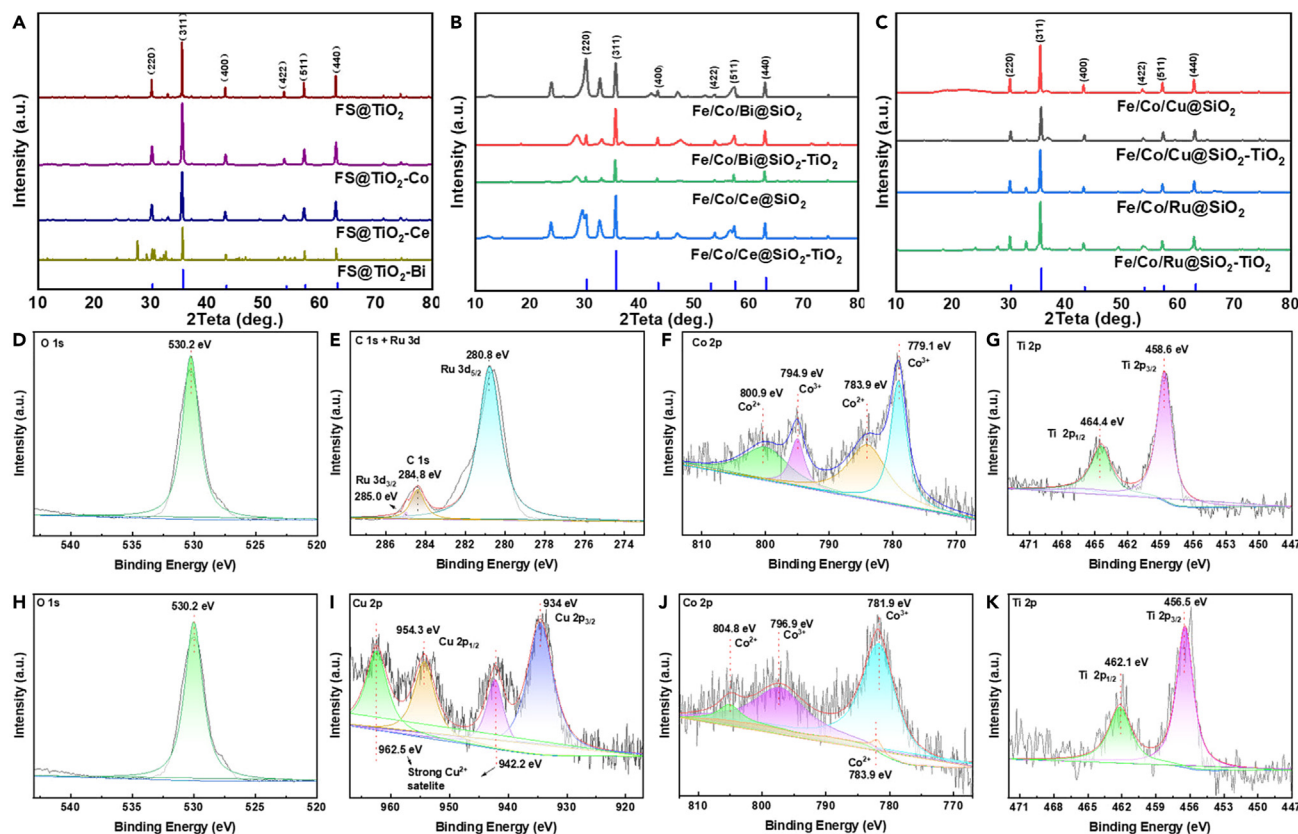
Figure 3. XRD and XPS spectra of catalysts

(A) X-ray powder diffraction patterns of four catalysts prepared by the sol-gel method (FS@TiO$_2$, FS@TiO$_2$–Bi, FS@TiO$_2$–Ce, and FS@TiO$_2$–Co).

(B–K) (B) and (C) X-ray powder diffraction patterns of eight catalysts prepared by the co-precipitation method [(B): FeCoBi@SiO$_2$, FeCoBi@SiO$_2$–TiO$_2$, FeCoCe@SiO$_2$, and FeCoCe@SiO$_2$–TiO$_2$; (C): FeCoCu@SiO$_2$, FeCoCu@SiO$_2$–TiO$_2$, FeCoRu@SiO$_2$, and FeCoRu@SiO$_2$–TiO$_2$]. Standards: Fe$_3$O$_4$(magnetite), PDF#75–0449; Bi$_2$O$_3$, PDF#78–1793; Ce$_2$O$_3$, PDF#78–0484; Co$_3$O$_4$, PDF#73–1701; CuO, PDF#45–0937, and RuO$_2$, PDF#02–1365. XPS spectra of O 1s (D), C 1s and Ru 3d (E), Co 2p (F), and Ti 2p (G) in FeCoRu@SiO$_2$–TiO$_2$. XPS spectra of O 1s (H), Cu 2p (I), Co 2p (J), Ti 2p (K) in FeCoCu@SiO$_2$–TiO$_2$.

vacancies greatly influence the catalytic performance, which could be an important contributor to the higher stability of the catalytic activity of calcined FeCoRu@SiO$_2$–TiO$_2$ compared with the catalyst that was not calcined. In FeCoCu@SiO$_2$–TiO$_2$, the O 1s peak (Figure 3H) as the same as the O 1s in FeCoRu@SiO$_2$–TiO$_2$. Doped Cu is the main reason of the ·OH produced. As shown in Figure 3I, the Cu 2p$_{3/2}$ peak and Cu 2p$_{1/2}$ peak were observed at 934.0 eV and 954.3 eV, respectively. Additionally, the peaks at 942.2 eV and 962.5 eV are strong Cu^{2+} satellite peak. Relation details between FeCoCu@SiO$_2$–TiO$_2$ and ·OH will be shown in subsequent mechanism part. The Co 2p (Figure 3J) and Ti 2p (Figure 3K) in FeCoCu@SiO$_2$–TiO$_2$ are likely with Co 2p and Ti 2p in FeCoRu@SiO$_2$–TiO$_2$. Besides, the Cu content in FeCoCu@SiO$_2$–TiO$_2$ is higher than Ru in FeCoRu@SiO$_2$–TiO$_2$ which results in the Co^{2+} peak at 783.9 eV (Figure 3J) being smaller than Co^{2+} peak at 783.9 eV in Figure 3F.

The magnetization saturation values of Fe$_3$O$_4$, FS@TiO$_2$, and FS@TiO$_2$–Co were 82.51, 50.72, and 40.34 emu·g^{-1}, respectively (Figure 4A). The order of FS@TiO$_2$–Co ≈ FS@TiO$_2$ < Fe$_3$O$_4$ was mainly attributed to SiO$_2$. The magnetization saturation values of FeCoRu, FeCoRu@SiO$_2$, and FeCoRu@SiO$_2$–TiO$_2$ were 44.98, 34.17, and 22.25 emu·g^{-1}, respectively (Figure 4B). The order of Fe$_3$O$_4$ > FeCoRu was attributed to CoO$_x$ and RuO$_x$, and the order of FeCoRu > FS@SiO$_2$ ≈ FS@SiO$_2$–TiO$_2$ was attributed to SiO$_2$.[46]

EPR is frequently used to evaluate the function of photocatalysts in photocatalytic processes that involve reactive oxygen species (Figures 4C and 4D). In this study, EPR with DMPO as the spin trapping agent was carried out to further verify the generation of superoxide radicals (·O$_2^-$).[47] Six peaks were observed for ·O$_2^-$, and peaks 1, 2, 4, and 6 were higher than peaks 3 and 5 (Figure 5C, red dashed line). Both FS@TiO$_2$–Co and FeCoRu@SiO$_2$–TiO$_2$ produced these peaks for ·O$_2^-$. The UV-visible results (Figure S4) showed that light in the UV and visible regions (λ < 800 nm) could be absorbed by FeCoRu@SiO$_2$–TiO$_2$.[48] Previous studies have shown that the band gap of anatase TiO$_2$ (3.23 eV) is larger than the band gap of FeCoRu@SiO$_2$–TiO$_2$. For FeCoRu@SiO$_2$–TiO$_2$, the absorption region is shifted toward a longer wavelength to allow for a UV and visible light response, which shows that modification with Ru and Co can reduce the band gap of FS@TiO$_2$–Co. These results show the FeCoRu@SiO$_2$–TiO$_2$ system absorbs the full spectrum of light and produces ·O$_2^-$ as a critical intermediate.[49] Comparing the black solid lines of FS@TiO$_2$–Co and FeCoRu@SiO$_2$–TiO$_2$, it is not difficult to find that FS@TiO$_2$–Co has more miscellaneous peaks than FeCoRu@SiO$_2$–TiO$_2$. According to the experiment results, the existence of miscellaneous peaks
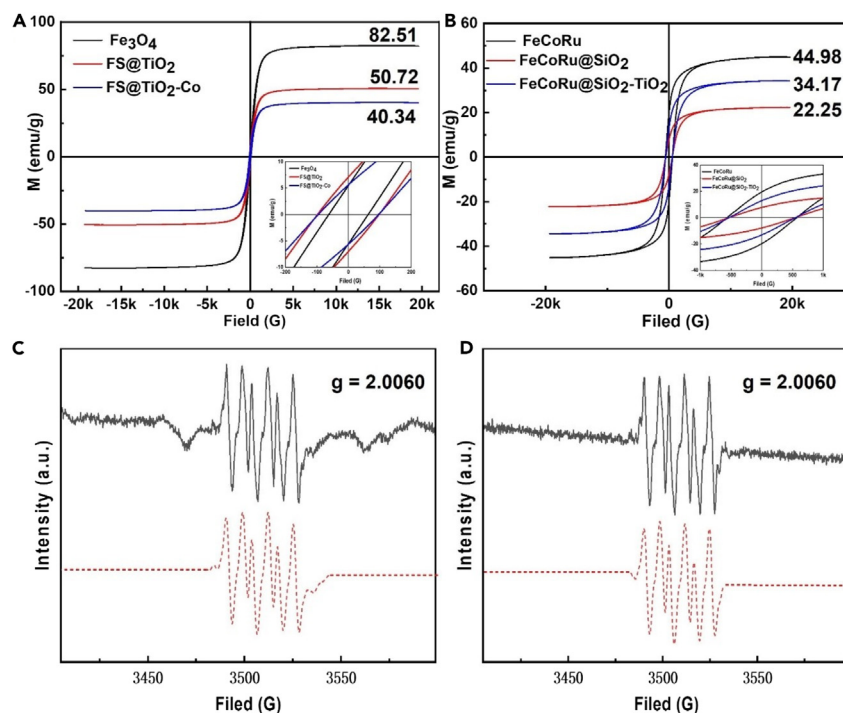
Figure 4. VSM spectra of catalysts and EPR spectra of FS@TiO$_2$-Co and FeCoRu@SiO$_2$-TiO$_2$

(A) Vibrating Sample Magnetometer (VSM) magnetization curves of Fe$_3$O$_4$, FS@TiO$_2$, and FS@TiO$_2$–Co catalysts.

(B) VSM magnetization curves of FeCoRu, FeCoRu@SiO$_2$, and FeCoRu@SiO$_2$–TiO$_2$.

(C and D) Electron paramagnetic resonance spectra of samples (black solid line) containing FS@TiO$_2$–Co (C) and FeCoRu@SiO$_2$–TiO$_2$ (D). Simulated (red dashed line) electron paramagnetic resonance spectra of DMPO/·O$_2^-$.

has negative impact to lignin model depolymerization which shows the radical aroused properties of FeCoRu@SiO$_2$–TiO$_2$ more than FS@TiO$_2$–Co.

Effect of reaction conditions on lignin model compound depolymerization

Photocatalysis of lignin was carried out under different conditions (Figure 5). The FeCoRu@SiO$_2$–TiO$_2$ (92.57%) catalyst gave a higher depolymerization efficiency (Figure 5A) than the other catalysts (Figures 5C–5E), which had efficiencies of 87.36% for FeCoCu@SiO$_2$–TiO$_2$, 88.75% for FeCoCe@SiO$_2$–TiO$_2$, 81.73% for FeCoBi@SiO$_2$–TiO$_2$, 61.05% for FS@TiO$_2$–Bi, 57.83% for FS@TiO$_2$–Ce, and 68.03% for FS@TiO$_2$–Co. The high Co content in the catalyst would be beneficial for breaking of the lignin C-O and C-C bonds.[50] The maximum yield of lignin model compound depolymerization products obtained with the FeCoRu@SiO$_2$–TiO$_2$ catalyst could be attributed to the presence of Ru, which enhanced C-O bond cleavage.[51] The minimum yield of lignin model compound depolymerization products was found in the reaction without a catalyst. For the catalytic oxidative depolymerization of lignin, catalysts synthesized by co-precipitation gave higher depolymerization rates than those synthesized by the sol-gel method.

A photocatalytic study was carried out with different solvents (methanol, ethanol, acetonitrile, dimethylformamide, water, and acetone [selected based on the previous research which showed a longest electron/holes lifetime[52]]). Depolymerization efficiencies of lignin with these solvents were evaluated at 60°C with irradiation at 230 W for 6 h. The results showed that the best solvent was acetone (Figure 5B). The minimum depolymerization efficiency occurred in water because of the poor solubility of lignin in this solvent, which indicated that good solubility was important for lignin degradation. The lignin model compound (2-phenoxy-1-phenylethanol) has a relatively low solubility in methanol and ethanol comparing to acetone. We take equal 2-phenoxy-1-phenylethanol (0.1000 ± 0.0020 g) in 20 mL methanol, ethanol, acetonitrile, dimethylformamide, water, and acetone. Standing for 5 h at room temperature, acetonitrile, dimethylformamide, and acetone can dissolve all lignin model compound. Combining with the depolymerization efficiency and HPLC-MS results, the results match the research of Qiu, Xueqing group,[53,54] Xiao, Rui group,[55,56] and Liu, Yunquan group.[57–59] All of the HPLC-MS results were shown in Figures 5C–5E.

The effects of different reaction conditions on lignin model compound depolymerization were investigated using HPLC-MS (Figures S5–S7). When the reaction time was increased from 1 h (44.495%) to 5 h (92.57%), the lignin model compound depolymerization efficiency increased (Figure 6A). The depolymerization efficiency at 1 h with the FeCoRu@SiO$_2$–TiO$_2$ catalyst was 44.49%, which was higher than that obtained without a catalyst (Figure 6A). When the reaction time was increased to 5 h, the depolymerization efficiency of lignin with the catalyst increased to 92.57%. With further increases in the reaction time to 6 or 7 h, the depolymerization efficiency did not show any further large
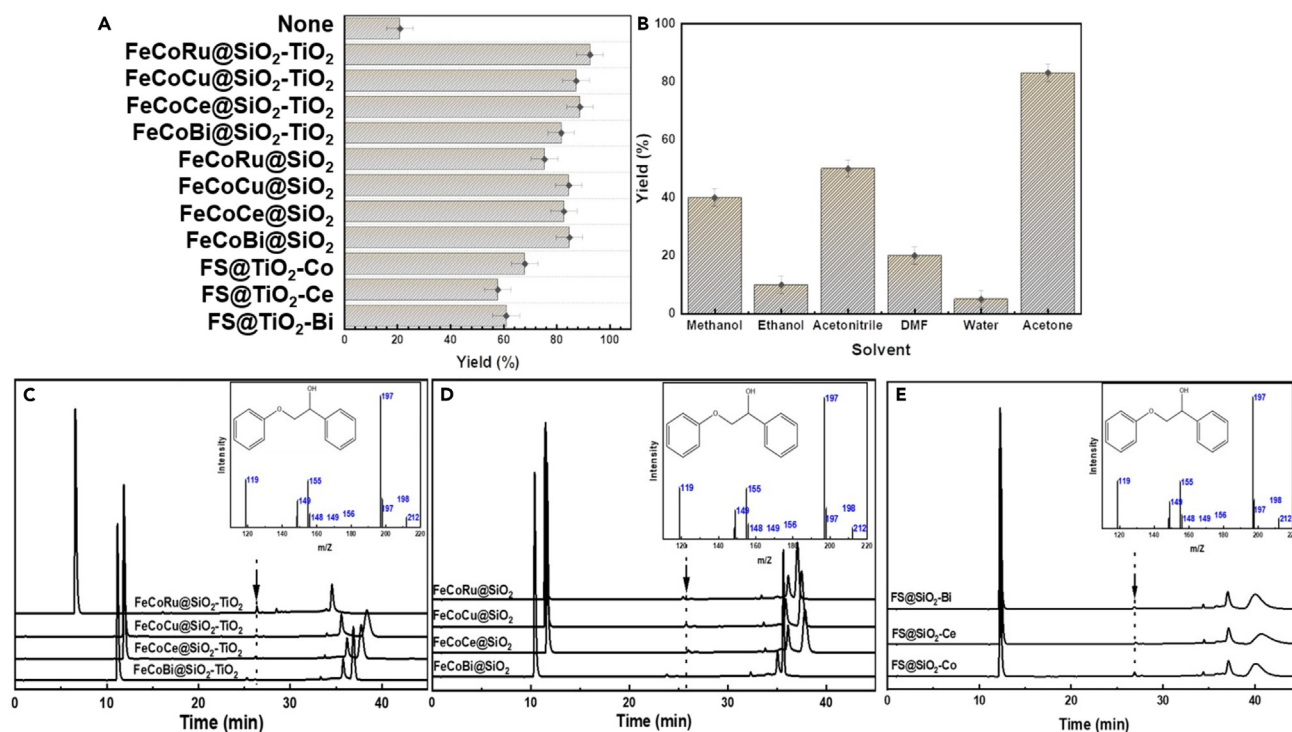
Figure 5. Screening of catalysts and solvents

(A–E) Effect of reaction conditions with different catalysts (A) and solvents (B) on the depolymerization efficiency, and high-performance liquid chromatography mass spectrometry results with different catalysts. Different solution of HPLC-MS after reaction, (C) FeCoRu@SiO$_2$–TiO$_2$, FeCoCu@SiO$_2$–TiO$_2$, FeCoCe@SiO$_2$–TiO$_2$, FeCoBi@SiO$_2$–TiO$_2$; (D) FeCoRu@SiO$_2$, FeCoCu@SiO$_2$, FeCoCe@SiO$_2$, FeCoBi@SiO$_2$; (E) FS@TiO$_2$–Bi, FS@TiO$_2$–Ce, FS@TiO$_2$–Co.

increases compared with that at 5 h. The results explained that with the time increase, reaction arrived at best depolymerization efficiency at 5 h. Therefore, 5 h reaction time was optimum for the lignin model compound depolymerization in lab condition. On the basis, further increasing the reaction was waste of electrical energy. However, at the natural light, we may need a longer time. Besides, if real lignin is used, we need a confirmed best time because the lignin depolymerization products monomers would reaggregate with the time increase.

The reaction was also conducted at different temperatures (30°C, 40°C, 50°C, 60°C, and 70°C). Increasing the reaction time from 30°C (32.498%) to 60°C (92.57%) greatly increased the lignin model compound depolymerization efficiency (Figure 6B). A small reduction in the depolymerization efficiency was observed when the temperature was increased to 70°C. To find the reason of low depolymerization lignin model compound efficiency at 70°C, we proceeded with a new experiment with a researcher observing the whole process. We found two possible reasons, which are as follows. (1) O^2 content: boiling point of acetone was 57°C. At 70°C, the solution appeared violently boiling phenomenon which would exorcise a part of O^2 from reactor results to reduce of O^2 content. Because of the violently boiling phenomenon, another proof was that the solution after reaction was only about 18.0 mL which verified the gas escapes in reaction process. Additionally, acetone steam was a challenge for the reactor tightness. (2) Radical and lignin model compound: because the solution was in a very unstable state, the radical was quickly quenched before touching the lignin model compound which reduced the efficiency of radical. The highest temperature we tested was 70°C because we would need a more airtight reactor to conduct the reaction at 80°C. Furthermore, high temperatures are not suitable for mild depolymerization.

Light irradiation at 140, 180, 210, 238, and 280 W was investigated for the lignin model compound depolymerization (Figure 6C). The depolymerization efficiency greatly increased from 61.52% at 140 W to 87.56% at 210 W. The depolymerization efficiency then decreased to 85.40% at 280 W. These results could be attributed to the photocatalyst properties.

According to these results, subsequent experiments were carried out with FeCoRu@SiO$_2$-TiO$_2$ under the following conditions: 60°C, 5 h, 210 W, and acetone as the solvent.

As shown in Figure 6D (before the reaction) and E (after the degradation) at the best conditions, it could clearly be seen that the reaction degraded the β-O-4 linkage (Figure 6F) quantitatively as the characteristic signals in the heteronuclear single quantum coherence (HSQC) almost disappeared. A$_β$ signal was still present, but only a part significantly reduced signal intensity. According to the previous research,[60–65] the B$_1$ was in accordance with the phenol, and the C$_α$ and C$_β$ were in accordance with the acetophenone. Combining the HPLC standard curve (the mentioned method was provided in supplementary materials: The plotting of HPLC standard curve), we obtained the final products yield (phenol [55.6%] and acetophenone [32.8%]) and lignin model compound depolymerization efficiency.
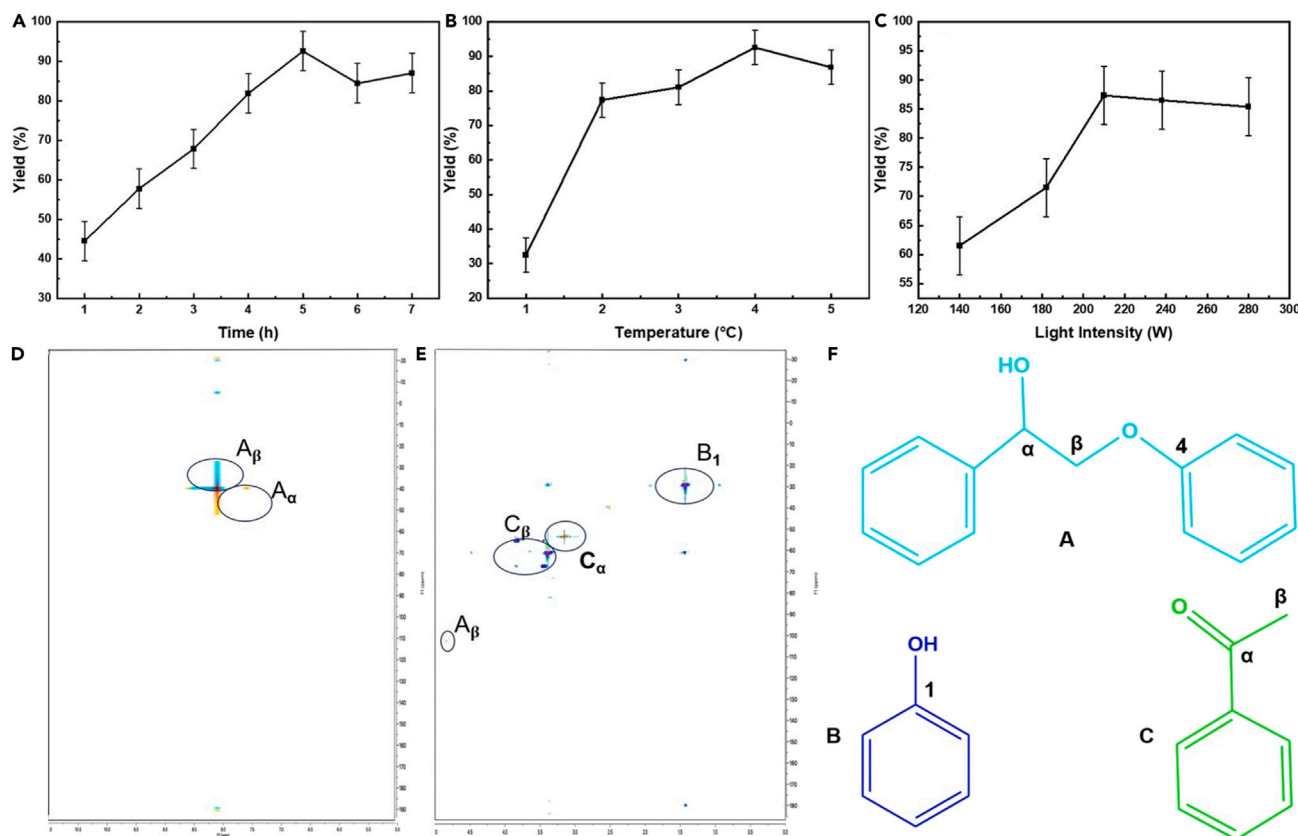
Figure 6. Single-factor anlysis of lignin model compound depolymerization

(A–F) Single-factor experiments for lignin model compound depolymerization: reaction time (A), temperature (B), and light intensity (C). 2D-NMR HSQC spectrum (in DMSO-d6) of lignin model compound; (D) before and (E) after 5 h reaction time; (F) exemplary structures for the β-O-4 aryl ether linkages (A), phenol (B) and acetophenone (C).

The radical mechanism of lignin model compound depolymerization

We investigated if DMPO/·O_2^- adducts were detected with the different catalysts. DMPO/·O^{2-} adduct showed the classic six peaks, and its characteristics showed that 3 and 5 peak were lower than 1, 2, 4, 6 peaks. DMPO/·OH adduct showed the classic quartet peaks, and its characteristics showed the ratio was 1: 2: 2: 1. The spectra of FS@SiO$_2$–Co showed superoxide radical[66] lines at 1 and 3 h, whereas FS@SiO$_2$–Bi and FS@SiO$_2$–Ce did not, which confirmed that Co gave a better response (Figure S8). Among the four co-precipitation catalysts, FeCoBi@SiO$_2$– TiO$_2$ and FeCoCe@SiO$_2$–TiO$_2$ showed the best depolymerization efficiencies because they contained Co (Figure S8). FeCoCu@SiO$_2$–TiO$_2$ produced hydroxyl radicals, which are stronger oxidants than OH but have a shorter lifetime. These results showed that CoO$_x$ and RuO$_x$ doping was beneficial for production of ·O_2^-, and that ·OH was produced with CuO$_x$ doping. For FeCoRu@SiO$_2$–TiO$_2$, ·O_2^- production was measured at 1, 2, 3, and 4 h. The FeCoRu@SiO$_2$–TiO$_2$ catalyst was selected for further investigation.

Because of the results presented in Figures 4C and 4D, real-time EPR was applied to investigate the radical signal strength at different reaction times. At 0 h without simulated sunlight, the photocatalyst did not produce radicals (Figure S9). At 2 h, in the radical initiation phase, a faint ·O_2^- signal was observed (Figure S9). As the time was gradually increased, the ·O_2^- signal increased until it reached a maximum at 4 h (Figure S9). According to Figure S10, at 0 h without simulated sunlight, the photocatalyst did not produce radicals (Figure S10). At 1 h, in the radical initiation phase, an obvious ·OH signal was observed (Figure S10). As the time was gradually increased, the ·O_2^- signal increased until it reached a maximum at 5 h (Figure S10). But at 3 h and 6 h, the existence of many miscellaneous peaks had a negative impact to reaction. Comparing the results between FeCoRu@SiO$_2$–TiO$_2$ and FeCoCu@SiO$_2$–TiO$_2$, we could find that the ·O_2^- radical was superior to ·OH. The firstly possible result was that the ·O_2^- had a long life than ·OH which could have a long action time in reaction. The secondly possible result was that in the middle time of reaction, miscellaneous peaks disturbed the reaction mechanism of ·OH.

According to the depolymerization efficiency and EPR results, we developed a possible mechanism for conversion of lignin containing the β-O-4 structure to aromatic monomers by the co-precipitation catalyst (Figure 7A).[67] All reactions were carried out in the customized dark chamber (Figure 7B). In the first phase, under simulated sunlight, the O$_2$ in the environment was oxidized by photogenerated holes on the photocatalyst surface, which formed ·O_2^- that could attack C-O bonds to form benzyl radical intermediates.[68] With bond energy decreasing from 55 to 7.8 kcal/mol, the benzyl radical intermediates were quickly broken to give the products.[68] In the second phase,
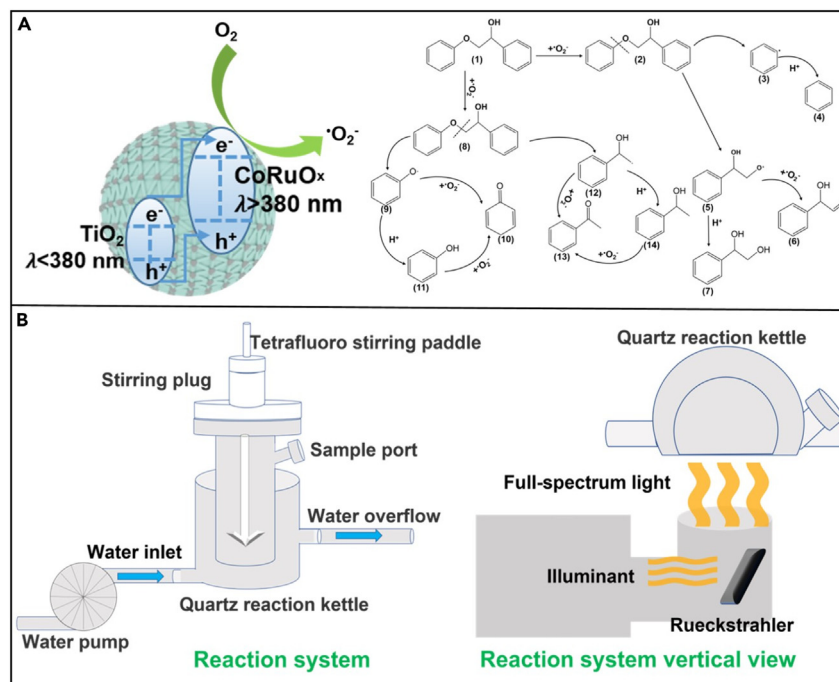
Figure 7. Possible reaction mechanism and reaction system diagram
(A and B) Probable mechanism of oxidative depolymerization of lignin model compound (A) and illustration of the photocatalytic reaction system (B).

when the O_2 in the solvent was exhausted, the content of $\cdot O_2^-$ decreased and the EPR signals of other radicals increased. The new radicals produced in system not only promoted lignin model compound depolymerization but also curbed the positive reaction,[67] which was directly reflected in the depolymerization efficiency. This photocatalytic cleavage of the lignin β-*O*-4 bond under mild conditions will have significance in engineering.

Conclusions

We successfully designed a series of microsphere catalysts using Fe_3O_4 and different metals. The Fe_3O_4 was used to make the catalyst magnetic, and SiO_2 was used as a coating to protect the Fe_3O_4 and other metal oxides from oxidation. Three metals (Co, Ce, and Bi) were evaluated, and the CoO_x-doped catalyst prepared by the sol-gel method performed better than the CeO_x-doped and BiO_x-doped catalysts. The results for these catalysts showed that the load of metal need to be increased and that it was very difficult to obtain a high depolymerization rate with a single metal catalyst. The co-precipitation method was used to successfully introduce two metals to the catalyst to utilize visible light, while retaining TiO_2 to absorb ultraviolet light. With this core-shell structure, we obtained a lignin model compound depolymerization rate of approximately 90%.

A photocatalytic oxidation mechanism illustrating the importance of $\cdot O_2^-$ was proposed. According to comparison of the different catalysts, the $\cdot O_2^-$ maybe the key to oxide lignin model compound depolymerization. We anticipate that these magnetic microsphere catalysts containing Co or Ru will provide a new strategy for selective cleavage of the lignin β-*O*-4 bond under mild conditions.

Limitations of the study

In this paper, we research the photocatalytic cleavage of β-*O*-4 bond. As is well known, high value-added lignin utilization still has a long way to go. We can further study the complex lignin model compound, such as lignin trimer model compound and real lignin. In future research, selectively breaking the C-O/C-C bond in real lignin is the key to obtain target chemicals. Additionally, to date, photocatalysts have been deeply developed. However, the efficiency selectivity of lignin depolymerization over full-spectrum light phototcatalysts is still low. A photocatalyst, which is more inexpensive, efficient, and stable, should be further developed.

STAR★METHODS

Detailed methods are provided in the online version of this paper and include the following:

- KEY RESOURCES TABLE
- RESOURCE AVAILABILITY

- ○ Lead contact
- ○ Materials availability
- ○ Data and code availability
- ● METHOD DETAILS
- ○ Experimental details
- ○ Depolymerization experiment details of lignin model compound
- ○ Characterization details
- ○ $\cdot O_2^-$ free radical experiments details

AUTHOR CONTRIBUTIONS

C.C.S.: conducted the experiments, conceptual framework proposing, writing original draft, writing-review and editing; W.L.: conceptual framework discussion, draft revising; S.L.: supervision, draft revising; C.H.M.: supervision, conceptual framework discussion, draft revising; S.X.L.: supervision, conceptual framework discussion.

DECLARATION OF INTERESTS

The authors declare no competing interests.

REFERENCES

1. Guo, H., Miles-Barrett, D.M., Zhang, B., Wang, A., Zhang, T., Westwood, N.J., and Li, C. (2019). Is oxidation–reduction a real robust strategy for lignin conversion? A comparative study on lignin and model compounds. Green Chem. *21*, 803–811. https://doi.org/10.1039/c8gc02670j.

2. Ku, C., Guo, H., Li, K., Wu, Q., and Yan, L. (2023). One-step fabrication of mesoporous sulfur-doped carbon nitride for highly selective photocatalytic transformation of native lignin to monophenolic compounds. Chem. Lett. *34*, 107298. https://doi.org/10.1016/j.cclet.2022.03.021.

3. Zhang, C., Shen, X., Jin, Y., Cheng, J., Cai, C., and Wang, F. (2023). Catalytic Strategies and Mechanism Analysis Orbiting the Center of Critical Intermediates in Lignin Depolymerization. Chem. Rev. *123*, 4510–4601. https://doi.org/10.1021/acs.chemrev.2c00664.

4. Fan, Y., Liu, C., Kong, X., Han, Y., Lei, M., and Xiao, H. (2022). A New Perspective on Polyethylene-Promoted Lignin Pyrolysis with Mass Transfer and Radical Explanation. Chem. Eng. J. *7*, 1318–1326. https://doi.org/10.1016/j.gee.2021.02.004.

5. Yogalakshmi, K.N., Poornima, D.T., Sivashanmugam, P., Kavitha, S., Yukesh, K.R., Sunita, V., AdishKumar, S., Gopalakrishnan, K., and Rajesh, B.J. (2022). Lignocellulosic Biomass-Based Pyrolysis: A Comprehensive Review. Chemosphere *286*, 131824. https://doi.org/10.1016/j.chemosphere.2021.131824.

6. Wolf, M.E., Hinchen, D.J., DuBois, J.L., McGeehan, J.E., and Eltis, L.D. (2022). Cytochromes P450 in the Biocatalytic Valorization of Lignin. Eltis. Curr. Opin. Biotech. *73*, 43–50. https://doi.org/10.1016/j.copbio.2021.06.022.

7. Chen, H., Wan, K., Zheng, F., Zhang, Z., Zhang, Y., Long, and Mechanism, D. (2021). Insight into Photocatalytic Conversion of Lignin for Valuable Chemicals and Fuels Production: A State-of-the-Art. Renew. Sust. Energ. Rev. *147*, 111217. https://doi.org/10.1016/j.rser.2021.111217.

8. Yang, C., Chen, H., Peng, T., Liang, B., Zhang, Y., and Zhao, W. (2021). Lignin Valorization toward Value-Added Chemicals and Fuels via Electrocatalysis: A Perspective. Chinese J. Catal. *42*, 1831–1842. https://doi.org/10.1016/S1872-2067(21)63839-1.

9. Song, Y., Motagamwala, A.H., Karlen, S.D., Dumesic, J.A., Ralph, J., Mobley, J.K., and Crocker, M. (2019). A comparative study of secondary depolymerization methods on oxidized lignins. Green Chem. *21*, 3940–3947. https://doi.org/10.1039/c9gc01663e.

10. Shelja, S., Sandeep, K., and Sasikumar, E. (2022). Chapter 19 - Photocatalysis of Biomass Lignin to Simple Aromatic Molecules. Biomass. Biofuel. Biochem. 535–561. https://doi.org/10.1016/B978-0-12-824419-7.00011-X.

11. Sandeep, K., Shelja, S., Senthil, M.A., Chirag, M., and Sasikumar, E. (2020). Biphasic separation approach in the DES biomass fractionation facilitates lignin recovery for subsequent valorization to phenolics. ACS Sustain. Chem. Eng. *8*, 19140–19154. https://doi.org/10.1021/acssuschemeng.0c07747.

12. Luo, N., Montini, T., Zhang, J., Fornasiero, P., Fonda, E., Hou, T., Nie, W., Lu, J., Liu, J., Heggen, M., et al. (2019). Visible-Light-Driven Coproduction of Diesel Precursors and Hydrogen from Lignocellulose-Derived Methylfurans. Nat. Energy *4*, 575–584. https://doi.org/10.1038/s41560-019-0403-5.

13. Wu, K., Cao, M., Zeng, Q., and Li, X. (2023). Radical and (Photo) Electron Transfer Induced Mechanisms for Lignin Photo- and Electro-Catalytic Depolymerization. Green Energy Environ. *8*, 383–405. http://creativecommons.org/licenses/by-nc-nd/4.0/.

14. Huang, Z., Luo, N., Zhang, C., and Wang, F. (2022). Radical Generation and Fate Control for Photocatalytic Biomass Conversion. Nat. Rev. Chem *6*, 197–214. https://www.researchgate.net/publication/358513966.

15. Li, C., Chen, R., Liang, Y., Dittrich, T., Pang, S., Zhao, Y., An, H., Zhang, G., and Fan, F. (2022). Spatiotemporal Imaging of Anisotropic Charge Transfer in Photocatalyst Particles. Nature *610*, 296–301. https://orcid.org/0000-0002-9301-7850.

16. Wu, X., Luo, N., Xie, S., Zhang, H., Zhang, Q., Wang, F., and Wang, Y. (2020). Photocatalytic transformations of lignocellulosic biomass into chemicals. Chem. Soc. Rev. *49*, 6198–6223. https://doi.org/10.1039/D0CS00314J.

17. Zou, W., Zhou, H., and Wang, M. (2023). Photoinduced biomimetic room-temperature C-O bond cleavage over Mn

doped CdS. ChemSusCheme202300727. https://doi.org/10.1002/cssc.202300727.

18. Zhang, J., Rajasekhar, B., and Yang, X. (2023). Novel 3D multi-layered carbon nitride/indium sulfide heterostructure for boosted superoxide anion radical generation and enhanced photocatalysis under visible light. Chem. Eng. J. 453, 139776. https://doi.org/10.1016/j.cej.2022.139776.

19. Gong, J., Imbault, A., and Farnood, R. (2017). The Promoting Role of Bismuth for the Enhanced Photocatalytic Oxidation of Lignin on Pt-TiO$_2$ under Solar Light Illumination. Appl. Catal., B 204, 296–303. https://doi.org/10.1016/j.apcatb.2016.11.045.

20. Almkhelfe, H., Li, X., Thapa, P., Hohn, K.L., and Amama, P.B. (2018). Carbon Nanotube-Supported Catalysts Prepared by a Modified Photo-Fenton Process for Fischer–Tropsch Synthesis. J. Catal. 361, 278–289. https://doi.org/10.1016/j.jcat.2018.02.009.

21. Liang, W., Li, J., and Jin, Y. (2012). Photo-Catalytic Degradation of Gaseous Formaldehyde by TiO$_2$/UV, Ag/TiO$_2$/UV and Ce/TiO$_2$/UV. Build. Environ. 51, 345–350. https://doi.org/10.1016/j.buildenv.2011.12.007.

22. Zhang, W., Shen, S., Zhang, Z., Huang, Y., Weng, Y., and Chen, G. (2020). Using One Photoredox Catalyst to Simultaneously Mediate Two Different Polymerizations for Photo-Triggered Multi-Component Orthogonal Polymerizations. Macromol. Rapid. Comm. 41, 2000373. https://doi.org/10.1002/marc.202000373.

23. Gao, X., Li, H., Wang, S., Liu, Z., Ma, J.F., Liu, X.E., and Song, G. (2022). Hydrodeoxygenation of Lignin Biophenolics to Cyclohexanes over Sub-Nanometric Ru Multifunctional Catalyst. Renew. Energy 201, 724–733. https://doi.org/10.1016/j.renene.2022.10.090.

24. Zhang, S., Jiang, X., Jiang, Y., Jiang, C., and Yao, X. (2023). Hybridization of CuO with BiVO$_4$ as an Efficient and Stable Photocatalyst for Selective Cleavage of Lignin C-C Bonds. Ind. Eng. Chem. Res. 62, 1277–1285. https://doi.org/10.1021/acs.iecr.2c03595.

25. Luo, N., Wang, M., Li, H., Zhang, J., Liu, H., and Wang, F. (2016). Photocatalytic Oxidation-Hydrogenolysis of Lignin β-O-4 Models via a Dual Light Wavelength Switching Strategy. ACS Catal. 6, 7716–7721. https://doi.org/10.1021/acscatal.6b02212.

26. Li, T., Wang, M., and Hao, Y. (2023). Highly Efficient Photodegradation of Magnetic GO-Fe$_3$O$_4$@SiO$_2$@CdS for Phenanthrene and Pyrene: Mechanism Insight and Application Assessment. Total Environ 857, 159254. https://doi.org/10.1016/j.scitotenv.2022.159254.

27. Zhou, Q., Luo, Z., Li, G., and Li, S. (2020). EPR Detection of Key Radicals during Coking Process of Lignin Monomer Pyrolysis. Anal. Appl. Pyrol. 152, 104948. https://doi.org/10.1016/j.jaap.2020.104948.

28. Patil, S.V., and Argyropoulos, D.S. (2017). Stable Organic Radicals in Lignin: A Review. ChemSusChem 10, 3284–3303. https://doi.org/10.1002/cssc.201700869.

29. Fang, Z., Li, F., Wang, M., Li, F., Wu, X., Fan, K., Tang, Q., Sun, L., and Zhang, P. (2023). Selective Electrocatalytic Upgrading of Lignin to Aryl Aldehydes and Carboxylic Acids over Dodecyl Sulfate-Intercalated CoS Nanocones. Appl. Catal., B 323, 122149. https://doi.org/10.1016/j.apcatb.2022.122149.

30. Zhang, C., and Wang, F. (2020). Catalytic Lignin Depolymerization to Aromatic Chemicals. Chem. Res. 53, 470–484. https://doi.org/10.1021/acs.accounts.9b00573.

31. Ozturk, D. (2022). Fe$_3$O$_4$/Mn$_3$O$_4$/ZnO-RGO Hybrid Quaternary Nano-Catalyst for Effective Treatment of Tannery Wastewater with the Heterogeneous Electro-Fenton Process: Process Optimization. Total Environ 828, 154473. https://doi.org/10.1016/j.scitotenv.2022.154473.

32. Hooshyari, K., Heydari, S., Beydaghi, H., and Rajabi, H.R. (2022). New Nanocomposite Membranes Based on Sulfonated Poly (Phthalazinone Ether Ketone) and Fe$_3$O$_4$@SiO$_2$@ Resorcinol–Aldehyde–SO$_3$H for PEMFCs. Renew. Energy 186, 115–125. https://doi.org/10.1016/j.renene.2021.12.074.

33. Asgharinezhad, A.A., Esmaeilpour, M., and Siavoshani, A.Y. (2022). Extraction and Preconcentration of Ni (Ii), Pb (Ii), and Cd (Ii) Ions Using a Nanocomposite of the Type Fe$_3$O$_4$@SiO$_2$@polypyrrole-Polyaniline. RSC Adv. 12, 19108–19114. https://doi.org/10.1039/d2ra03077b.

34. Han, K.H., Kim, Y.H., Pak, I.H., Yu, J.H., Ho, I.C., and Han, R.H. (2022). Fe$_3$O$_4$@SiO$_2$@TiO$_2$@PDA Nanocomposite for the Degradation of Organic Materials. Chem. Eng. Technol. 45, 178–188. https://doi.org/10.1002/ceat.202100484.

35. Ghasemzadeh, B., Matin, A.A., Habibi, B., and Ebadi, M. (2022). Cotton/Fe$_3$O$_4$@SiO$_2$@H$_3$PW$_{12}$O$_{40}$ a magnetic heterogeneous catalyst for biodiesel production: Process optimization through response surface methodology. Ind. Crops Prod. 12, 19108–19114. https://doi.org/10.1016/j.renene.2021.12.074.

36. Cahyana, A.H., Liandi, A.R., Maghdalena, M., Yunarti, R.T., and Wendari, T.P. (2022). Magnetically Separable Fe$_3$O$_4$/Graphene Oxide Nanocomposite: An Efficient Heterogenous Catalyst for Spirooxindole Derivatives Synthesis. Ceram. Int. 48, 18316–18323. https://doi.org/10.1016/j.ceramint.2022.03.090.

37. Sun, W., Li, Q., Gao, S., and Shang, J.K. (2012). Monometallic Pd/Fe$_3$O$_4$ Catalyst for Denitrification of Water. Appl. Catal., B 125, 1–9. https://doi.org/10.1016/j.apcatb.2012.05.014.

38. Li, T., Gu, F., Chen, X.H., Zhang, Q., Fu, H.C., Luo, H.Q., and Li, N.B. (2023). Engineered Superhydrophilic/Superaerophobic Catalyst: Two-Dimensional Co (OH)$_2$-CeO$_2$ Nanosheets Supported on Three-Dimensional Co Dendrites for Overall Water Splitting. Inorg. Chem. 62, 2784–2792. https://doi.org/10.1021/acs.inorgchem.2c03910.

39. Peng, X., Xian, X., Han, L., Liu, Y., Zheng, P., Fu, Y., Dong, P., Zeng, X., and Zhang, Y. (2023). Co$_2$P Nanoparticles Encapsulated in N-Doped Carbon Nanotubes as a Bifunctional Oxygen Catalyst for a High-Performance Rechargeable Zn-Air Battery. ACS Appl. Nano Mater. 6, 2027–2034. https://doi.org/10.1021/acsanm.2c05035.

40. Zhao, Q., Zhang, Y., Liu, Q., Song, C., Lu, X., Ma, J., Wang, L., and He, H. (2023). Boosting the Catalytic Performance of Volatile Organic Compound Oxidation Over Platelike MnO$_2$/CoAlO Catalyst by Weakening the Co-O Bond and Accelerating Oxygen Activation. ACS Catal. 13, 1492–1502. https://doi.org/10.1021/acscatal.2c04680.

41. Cai, G., Xiong, W., Zhou, S., Liu, P., Lv, Y., Hao, F., Luo, H., and Kong, C. (2022). A Multi-Functional Ru Mo Bimetallic Catalyst for Ultra-Efficient C$_3$ Alcohols Production from Liquid Phase Hydrogenolysis of Glycerol. J. Chem. Eng. 51, 199–215. https://doi.org/10.1016/j.cjche.2021.09.013.

42. Luo, B., Zhou, L., Tian, Z., He, Y., and Shu, R. (2022). Hydrogenolysis of Cornstalk Lignin in Supercritical Ethanol over N-Doped Micro-Mesoporous Biochar Supported Ru Catalyst. Fuel Process. Technol. 231, 107218. https://doi.org/10.1016/j.fuproc.2022.107218.

43. Zou, H., and Chen, J. (2022). Efficient and Selective Approach to Biomass-Based Amine by Reductive Amination of Furfural Using Ru Catalyst. Appl. Catal., B 309, 121262. https://doi.org/10.1016/j.apcatb.2022.121262.

44. Zhou, S., Jang, H., Qin, Q., Hou, L., Kim, M.G., Liu, S., Liu, X., and Cho, J. (2022). Boosting Hydrogen Evolution Reaction by Phase Engineering and Phosphorus Doping on Ru/P-TiO$_2$. Angew. Chem. Int. Edit. 61, e202212196. https://doi.org/10.1002/anie.202212196.

45. Shelja, S., Sandeep, K., Senthil, M.A., and Sasikumar, E. (2023). Promising photocatalytic degradation of lignin over carbon quantum dots decorated TiO$_2$ nanocomposite in aqueous condition. Appl. Cata. A-Gen. 602, 117730. https://doi.org/10.1016/j.apcata.2020.117730.

46. Wang, H., Zhang, C., Zhang, X., Wang, S., Xia, Z., Zeng, G., Ding, J., and Ren, N. (2022). Construction of Fe$_3$O$_4$@β-CD/g-C$_3$N$_4$ Nanocomposite Catalyst for Degradation of PCBs in Wastewater through Photodegradation and Heterogeneous Fenton Oxidation. Chem. Eng. J. 429, 132445. https://doi.org/10.1016/j.cej.2021.132445.

47. Zhang, Y., Richards, D.S., Grotemeyer, E.N., Jackson, T.A., and Schöneich, C. (2022). Near-UV and Visible Light Degradation of Iron (III)-Containing Citrate Buffer: Formation of Carbon Dioxide Radical Anion via Fragmentation of a Sterically Hindered Alkoxyl Radical. Mol. Pharm. 19, 4026–4042. https://doi.org/10.1021/acs.molpharmaceut.2c00501.

48. Zuo, S., Zhang, H., Li, X., Han, C., Yao, C., and Ni, C. (2022). Dual Active Sites Boosting Photocatalytic Nitrogen Fixation over Upconversion Mineral Nanocomposites under the Full Spectrum. ACS Sustain Chem. Eng. 10, 1440–1450. https://doi.org/10.1021/acssuschemeng.1c06474.

49. Davaritouchaee, M., Hiscox, W.C., Terrell, E., Mancini, R.J., and Chen, S. (2020). Mechanistic Studies of Milled and Kraft Lignin Oxidation by Radical Species. Green Chem. 22, 1182–1197. https://doi.org/10.1039/C9GC04162A.

50. Zhu, Y., Zhao, Y., Song, W., He, Z., Yao, R., and Deng, Z. (2023). Metal Supported Hydrotalcite Catalytic Depolymerization of Lignin: Effects of Reaction Parameter on Compounds Distribution. Fuel 340, 127559. https://doi.org/10.1016/j.fuel.2023.127559.

51. Zhong, Z., Li, J., Jian, M., Shu, R., Tian, Z., Wang, C., Chen, Y., Shi, N., and Wu, Y. (2023). Hydrodeoxygenation of Lignin-Derived Phenolic Compounds over Ru/TiO$_2$ Catalyst: Effect of TiO$_2$ Morphology. Fuel 333, 126241. https://doi.org/10.1016/j.fuel.2022.126241.

52. Shelja, S., Sandeep, K., Senthil, M.A., Muthukumaran, P., Vijayakumar, S., and Sasikumar, E. (2021). Nb$_2$O$_5$/g-C$_3$N$_4$ Heterojunction facilitates 2,5-Diformylfuran production via photocatalytic oxidation of

5-Hydroxymethylfurfural under direct sunlight irradiation. ChemPhotoCHem 5, 1–11. https://doi.org/10.1002/cptc.202100199.

53. Ouyang, X., Ruan, T., and Qiu, X. (2016). Effect of solvent on hydrothermal oxidation depolymerization of lignin for the production of monophenolic compounds. Fuel Process. Technol. 144, 181–185. https://doi.org/10.1016/j.fuproc.2015.12.019.

54. Zhu, G., Ouyang, X., Yang, Y., Ruan, T., and Qiu, X. (2016). Selective cleavage of aryl ether bonds in dimeric lignin model compounds. RSC Adv. 6, 17880–17887. https://doi.org/10.1039/c5ra26235f.

55. Liu, C., Hu, J., Zhang, H., and Xiao, R. (2016). Thermal conversion of lignin to phenols: Relevance between chemical structure and pyrolysis behaviors. Fuel 182, 864–870. https://doi.org/10.1016/j.fuel.2016.05.104.

56. Liu, C., Wang, X., Lin, F., Zhang, H., and Xiao, R. (2018). Structural elucidation of industrial bioethanol residual lignin from corn stalk: A potential source of vinyl phenolics. Fuel Process. Technol. 169, 50–57. https://doi.org/10.1016/j.fuproc.2017.09.008.

57. Cheng, C., Li, P., Yu, W., Shen, D., Jiang, X., and Gu, S. (2020). Nonprecious metal/bimetallic catalytic hydrogenolysis of lignin in a mixed-solvent system. ACS Sustain. Chem. Eng. 8, 16217–16228. https://doi.org/10.1021/acssuschemeng.0c05362.

58. Cheng, C., Li, P., Yu, W., Shen, D., and Gu, S. (2021). Catalytic hydrogenolysis of lignin in ethanol/isopropanol over an activated carbon supported nickel-copper catalyst. Bioresour. Technol. 319, 124238. https://doi.org/10.1016/j.biortech.2020.124238.

59. Cheng, C., Julianne, T., Jacob, A.B., Shen, D., Mahdi, M.A., and Peter, C.F. (2020). Hydrogenolysis of organosolv lignin in ethanol/isopropanol media without added transition-metal catalyst. ACS Sustain. Chem. Eng. 8, 1023–1030. https://doi.org/10.1021/acssuschemeng.9b05820.

60. Chen, C., Ewellyn, A.C., and Hanna, S.G. (2003). Reaction mechanisms in delignification of pine kraft-AQ pulp with hydrogen peroxide using Mn (IV)-Me4DTNE as catalyst. J. Agnic. Food. Chem. 51, 1932–1941. https://doi.org/10.1021/jf020992n.

61. Jakob, M., Torsten, R., Claire, B., Julien, B., and Carsten, B. (2015). Iron-catalysed oxidative cleavage of lignin and β-O-4 lignin model compounds with peroxides in DMSO. Green Chem. 17, 5001. https://doi.org/10.1039/c5gc01306b.

62. Du, X., Marta, P., Carmen, F., Jorge, R., José, C.d.R., Jesús, J., Li, J., Ana, G., and Angel, T.M. (2014). Analysis of lignin–carbohydrate and lignin–lignin linkages after hydrolase treatment of xylan–lignin, glucomannan–lignin and glucan–lignin complexes from spruce wood. Planta 239, 1079–1090. https://doi.org/10.1007/s00425-014-2037-y.

63. Zhao, C., Huang, J., Yang, L., Yue, F., and Lu, F. (2019). Revealing structural differences between alkaline and kraft lignins by HSQC NMR. Ind. Eng. Chem. Res. 58, 5707–5714. https://doi.org/10.1021/acs.iecr.9b0049.

64. Jorge, R., Ana, G., Lidia, N., Jiménez-Barbero, J., Craig, B.F., Hoon, K., John, R., Angel, T.M., and Jose, C.d.R. (2011). Lignin composition and structure in young versus adult eucalyptus globulus plants. Plant Physiol 155, 667–682. https://doi.org/10.1104/pp.110.167254.

65. Zhao, C., Li, S., Zhang, H., Yue, F., and Lu, F. (2020). Structural insights into the alkali lignins involving the formation and transformation of arylglycerols and enol ethers. Int. J. Biol. Macromol. 152, 411–417. https://doi.org/10.1016/j.ijbiomac.2020.02.241.

66. Wierzbicki, S., Douglin, J.C., Singh, R.K., Dekel, D.R., and Kruczała, K. (2023). Operando EPR Study of Radical Formation in Anion-Exchange Membrane Fuel Cells. ACS Catal. 13, 2744–2750. https://doi.org/10.1021/acscatal.2c05843.

67. Zeng, J., Tong, Z., Bao, H., Chen, N., Wang, F., Wang, Y., and Xiao, D. (2020). Controllable Depolymerization of Lignin Using Carbocatalyst Graphene Oxide under Mild Conditions. Fuel 267, 117100. https://doi.org/10.1016/j.fuel.2020.117100.

68. Xu, J., Li, M., Qiu, J., Zhang, X.F., and Yao, J. (2021). Fine Tuning of Cd_xZn_1-XS for Photo-Depolymerization of Alkaline Lignin into Vanillin. Int. J. Biol. Macromol. 185, 297–305. https://doi.org/10.1016/j.ijbiomac.2021.06.104.

STAR★METHODS

KEY RESOURCES TABLE

REAGENT or RESOURCE	SOURCE	IDENTIFIER
Chemicals, peptides, and recombinant proteins		
Absolute ethanol	Aladdin	CAS: 64-17-5
Tetrabutyl titanate	Aladdin	CAS:5593-70-4
Tetraethyl orthosilicate	Aladdin	CAS:78-10-4
5,5-dimethyl-1-pyrroline N-oxide (DMPO)	Aladdin	CAS:3317-61-1
2-phenoxy-1-phenylethanol	Aladdin	CAS:60-12-8
Cobalt nitrate hexahydrate	Macklin	CAS:10026-22-9
Iron (II, III) oxide	Macklin	CAS:1309-37-1
Bismuth (III) nitrate pentahydrate	Macklin	CAS:10035-06-0
Cerium (III) nitrate hexahydrate	Macklin	CAS:10108-73-3
Copper nitrate trihydrate	Macklin	CAS:10031-43-3
Ruthenium (III) chloride hydrate	Macklin	CAS:14898-67-0
Acetone	Macklin	CAS:67-64-1
Other		
X-ray Diffractometer (XRD)	Rigaku Ultima IV	
Scanning Electron Microscope (SEM)	FEI Inspect F50 instrument	
Energy Dispersive Spectroscopy (EDS)	EDAX Octane system	
X-ray Photoelectron Spectroscopy (XPS)	Axis Ultra^{DLD} (Kratos)	
Transmission Electron Microscope (TEM)	FEI Talos F200x	
Fourier Transform Infrared Spectroscopy (FT-IR)	IS10 (Nicolet)	
Ultraviolet–visible Spectroscopy (UV-vis)	UV-2450 (Shimadzu)	
Electron Paramagnanetic Resonance (EPR)	Bruker ELEXSYS II E 500	

RESOURCE AVAILABILITY

Lead contact

Further information for resources and regents could be directed to and will be fulfilled by the lead contact, Chunhui Ma (mchmchmchmch@163.com).

Materials availability

This study does not generate new unique reagents.

Data and code availability

All requested data is available in this paper will be shared by the lead contact upon request.
This paper does not report original code.
Any additional information required to reanalyze the data reported in this paper is available from the lead contact upon request.

METHOD DETAILS

Experimental details

The photocatalytic reaction was carried out in a reactor with a capacity of 50 mL. The reactor was equipped with a super thermostatic water circulation system for maintaining the temperature. A 230 W xenon lamp was used for irradiation with full-spectrum light to simulate sunlight. The quartz reactor had one port for withdrawal of the sample. Additionally, the system was coupled with a mechanical stirrer for constant mixing of reactants.

Depolymerization experiment details of lignin model compound

A dark chamber was prepared for photocatalytic depolymerization of lignin model compound. Hot water was circulated using a water pump, which controlled the reaction temperature. A quartz kettle was used for the reaction. The kettle had a sampling port, a stirring plug for setting tetrafluoro stirring rod, stirring paddle, and water port for temperature control. Full-spectrum light (HPRS-PEC250, Zhongjiaojinyuan) was reflected into the quartz reaction kettle by a reflector.

Characterization details

XRD was conducted using a Rigaku Ultima IV X-ray diffractometer with Cu Kα radiation (1.5418 nm) at 40 kV and 40 mA. SEM was performed using a FEI Inspect F50 instrument, and energy dispersive spectroscopy (EDS) was performed using an EDAX Octane system. *In situ* XPS characterization was conducted using an Axis Ultra^{DLD} (Kratos) equipped with an Al Kα excitation source (1486.6 eV) and with C as the internal standard (C 1s = 284.80 eV). TEM was conducted using a FEI Talos F200x. FT-IR was conducted using a IS10 (Nicolet) with smart iTR attachment and the testing wavelength from 400 to 4000 cm^{-1}. UV-vis was conducted using a UV-2450 (Shimadzu) and the testing wavelength from 200 to 800 cm^{-1}.

$\cdot O_2^-$ free radical experiments details

Our studies with metal oxides suggested that $\cdot O_2^-$ was likely generated during the reaction. DMPO was used to detect $\cdot O_2^-$. EPR was performed at room temperature using a Bruker ELEXSYS II E 500. Real-time detection method: When the temperature arriving to 60°C, before light irradiation, taking 0.1 mL 2-phenoxy-1-phenylethanol solution and mixing with 0.1 mL DMPO solution (concentration:1 mg/mL, DMPO solution was prepared in advance) as 0 h sample. After light irradiation, taking 0.1 mL reaction solution interval every 1 h until 7 h reaction time. Finally, using the same method of 0 h sample, 8 samples (0 h, 1 h, 2 h,3 h, 4 h, 5 h, 6 h, 7 h) were obtained. It was worth noting that the EPR testing equipment should be near our reaction system to ensure every sample to be detected within 3 min.